MATERIALS CHEMISTRY FRONTIERS

CHINESE CHEMICAL SOCIETY

ROYAL SOCIETY OF CHEMISTRY

RESEARCH ARTICLE

View Article Online
View Journal

Cite this: DOI: 10.1039/d2qm00866a

Blue photoluminescence enhancement achieved by zero-dimensional organic indium halides *via* a metal ion doping strategy†

Fang Lin,[a] Guicheng Yu,[a] Shuchen Weng,[a] Chao Zhou,[ab] Yonglei Han,[ab] Wei Liu,[c] Kang Zhou,[a] Yongfei Wang[b] and Haoran Lin*[a]

Received 26th August 2022,
Accepted 4th November 2022

DOI: 10.1039/d2qm00866a

rsc.li/frontiers-materials

Low-dimensional organic–inorganic metal halide hybrids exhibit promising optical properties for light emitting applications. However, developing lead-free blue-light emitters with high photoluminescence quantum efficiency (PLQE) remains an ongoing challenge. In our work, a novel zero-dimensional (0D) indium hybrid compound $(MA)_4InCl_7$ (MA = $CH_3NH_3^+$) was developed which exhibited broadband blue emission with a PLQE of 11.2% when excited by ultraviolet (UV) light. More interestingly, upon Cs^+ or Mn^{2+} doping, the emission of the 0D compound further blue-shifted and became narrower, while the PLQE was significantly enhanced to 18.8% (Cs^+) or 20.7% (Mn^{2+}). More prominent PLQE enhancement to 74.7% was observed after Sb^{3+} doping, which also altered the emission spectrum to the orange region. According to experimental characterization and theoretical calculations, we attribute the PLQE enhancement upon Cs^+ and Mn^{2+} doping to defect passivation and the orange emission upon Sb^{3+} doping to altered emission centers. We have demonstrated that multiple metal ions possess the ability to improve the light emitting properties of 0D organic–inorganic metal halides, and $(MA)_4InCl_7$ could be utilized as a Sb^{3+} heavy metal ion sensor with high selectivity and sensitivity.

Introduction

Organic–inorganic metal halides (OIMHs) are a class of materials which are employed in a variety of optoelectronic devices such as solar cells, light-emitting diodes, detectors and lasers.[1–7] Among them, low-dimensional lead-free OIMHs have received considerable research attention as stable and environmentally friendly light-emitting materials.[8,9] Lowering the structural dimensionality of OIMHs from three-dimension (3D) to low-dimension significantly enhances the exciton–phonon coupling through quantum confinement and dielectric confinement effects, thus giving rise to the formation of self-trapped excitons (STEs) and representative highly efficient broadband emissions with a large Stokes shift.[10]

Zero-dimensional (0D) OIMHs comprising isolated inorganic polyhedrons and organic cations possess high structural versatility, color tunability and high photoluminescence quantum efficiency (PLQE) due to their quantum-confined structures, making them promising materials for luminescence applications.[11] For example, a series of 0D hybrid materials, such as $(C_5H_{14}N_3)_2MnBr_4$,[12] $(C_{10}H_{16}N)_2MnBr_4$,[13] $(TMA)_2SbCl_5{\cdot}DMF$,[14] $(MePPh_3)_2SbCl_5$,[15] $(C_{12}H_{28}N)_2SbCl_5$,[16] and $(C_4N_2H_{14}Br)_4SnBr_6$,[17] were developed with various emission colors and near-unity PLQEs. To achieve the three primary colors, blue-emissive 0D OIMHs were also reported, mostly lead-containing compounds such as $(BAPrEDA)PbCl_6{\cdot}(H_2O)_2$,[18] $(C_{13}H_{19}N_4)_2PbBr_4$,[19] and $(C_9NH_{20})_7(PbCl_4)Pb_3Cl_{11}$.[20] However, the toxicity of lead limits their development and applications. Lead-free blue emitters were developed using all-inorganic materials in which alkali copper(I) halides such as $Cs_3Cu_2X_5$,[21–23] Rb_2CuX_3,[24] and K_2CuX_3[25] have shown extraordinary PLQYs of up to 100%. On the other hand, lead-free 0D OIMHs have also been massively investigated in recent years.[26,27] Several reports suggest that the substitution of lead by indium is an effective strategy to develop lead-free blue emitters. For example, the PLQE of blue-emissive $(C_7H_8N_6)InCl_9$ with a long lifetime of 1.2 s can be enhanced from 25.2% to 42.8% upon illumination.[28] $BAPP^{4+}$-associated blue emission in $BAPPIn_2Cl_{10}$ endows it with intriguing afterglow properties.[29] $TpyInCl_x$ (x = 3 or 5) emitters were tuned to be blue-emissive and with an

[a] Hoffmann Institute of Advanced Materials, Shenzhen Polytechnic, 7098 Liuxian Blvd, Nanshan District, Shenzhen, 518055, China. E-mail: hlin@szpt.edu.cn
[b] School of Materials and Metallurgy, University of Science and Technology Liaoning, 185 Qianshan Zhong Road, Anshan, 114051, China
[c] School of Chemical Engineering and Technology, Sun Yat-Sen University, Zhuhai, 519000, China

† Electronic supplementary information (ESI) available: Experimental section, crystallographic data, PXRD patterns, TGA data, UV-vis absorption spectra and PL spectra. CCDC 2195355–2195358. For ESI and crystallographic data in CIF or other electronic format see DOI: https://doi.org/10.1039/d2qm00866a

increased PLQE of up to 47.66% by regulating the polarity of the solvent.[30] $[H_2EP]_2InCl_6{\cdot}Cl{\cdot}H_2O{\cdot}C_3H_6O$ and $[H_3AEP]InCl_6{\cdot}H_2O$ peaking at 430 nm displayed a PLQY of 13.44% and 4.12%, respectively.[31] $(C_{14}H_{22}N)InBr_4$, isolated tetrahedral $[InBr_4]^-$ separated by organic ligands, showed a visibly bright blue emission with a PLQE of 16.36%.[32] Despite the recent advances of 0D indium OIMH blue emitters, their poor stability and relatively low PLQEs still remain problematic.

For low-dimensional OIMHs, metal ion doping is considered as an attractive and effective strategy to optimize their photoluminescence properties and enhance their stability. There are also several cases of doping Sb^{3+} in 0D indium OIMHs to simultaneously manipulate the emission spectrum and enhance the PLQE. Upon rational control of the Sb amount, both near-unity PLQEs and a bright white-light emission were achieved in $(C_7H_8N_6)InCl_9$,[28] $BAPPIn_2Cl_{10}$,[29] $(C_8NH_{12})_6InBr_9{\cdot}H_2O$[33] and $InCl_7(C_4H_{10}SN_4)$.[34] However, as far as we know, there are no reports on using metal ions other than Sb^{3+} to dope 0D indium OIMHs. The light-emitting mechanism upon ion doping is less explored. Also, exploration of the applications of metal ion doped 0D indium compounds is limited besides Kuang's[29] and Chen's[34] recent works which suggest that antimony doped indium compounds could be used as anti-counterfeiting materials and solvent sensors.

Here, we have synthesized a lead-free 0D indium-based OIMH $(MA)_4InCl_7$ ($MA = CH_3NH_3^+$), which exhibits a bright broadband blue emission peaked at 455 nm with a PLQE of 11.2%. The metal ion doping strategy was applied to this material and a series of compounds including $(MA)_4InCl_7{:}Cs^+$, $(MA)_4InCl_7{:}Mn^{2+}$ and $(MA)_4InCl_7{:}Sb^{3+}$ were obtained. Reduced full width at half maxima (FWHM) and increased PLQE (from 11.2% to 20.7%) have been achieved through introducing Cs^+ or Mn^{2+} into the pristine material. Upon Sb^{3+} doping, $(MA)_4InCl_7{:}Sb^{3+}$ exhibits significantly shifted orange STE emission and a greatly enhanced PLQE of up to 74.7%, which makes it a perfect sensor for Sb^{3+} ion sensing.

Results and discussion

Single crystals of $(MA)_4InCl_7$ and the doped compounds were grown *via* a solvothermal method (see the ESI† for details). The feeding ratios were selected to achieve the maximum PLQEs (Fig. S1 and Table S5, ESI†) and the following characterization is based on these feeding ratios. The single crystal structures of $(MA)_4InCl_7$ and the doped ones were determined by single crystal X-ray diffraction (SCXRD) and the crystallographic details are listed in Table S1 (ESI†). As shown in Fig. 1, the 0D crystallographic structure of $(MA)_4InCl_7$ adopts a *P*2/*n* space group, which can be regarded as individual $InCl_6^{3-}$ octahedra embedded periodically in the matrix comprising $CH_3NH_3^+$ and Cl^- ions. Interestingly, there are two geometrically different inorganic octahedra, named $[In(1)Cl_6]^{3-}$, and $[In(2)Cl_6]^{3-}$, respectively. We calculated the extent of distortion of

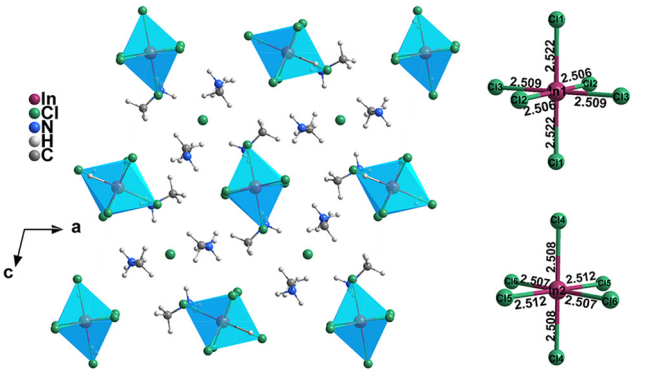

Fig. 1 Crystal structure of 0D $(MA)_4InCl_7$ and the In–Cl bond lengths of the $[InCl_6]^{3-}$ octahedron.

two $[InCl_6]^{3-}$ octahedra based on In–Cl bond lengths and Cl–In–Cl bond angles by the following equations:[35]

$$\lambda_{oct} = \frac{1}{6}\sum_{i=1}^{6}\left(\frac{d_i - d}{d}\right)^2$$

$$\sigma^2_{oct} = \frac{1}{11}\sum_{i=1}^{12}(\theta_i - 90^\circ)^2$$

where d is the average In–Cl bond length, d_i is the length of each of the six In–Cl bonds, and θ_i is the angle of each of the twelve bonds of the octahedron in Tables S2 and S3 (ESI†).

The calculated extent of distortion ($\lambda_{oct1} = 7.21 \times 10^{-6}$, $\lambda_{oct2} = 6.82 \times 10^{-7}$; $\sigma^2_{oct1} = 0.271$, $\sigma^2_{oct2} = 0.264$) is much smaller than those of the reported Sn^{2+}-, Bi^{3+}-, and Sb^{3+}-based OIMHs because of the strongly antibonding nature of the ns orbitals of the later ones.[36,37] In addition, the lattice parameters (Table S1, ESI†) and the extent of distortion of $InCl_6^{3-}$ for all doped compounds (Table S4, ESI†) are similar to those of the pristine compound, which indicate that a small amount of metal doping do not alter the crystal structure significantly. It is worth mentioning that Cs^+ is observable in the experimental crystal structure of $(MA)_4InCl_7{:}Cs^+$ in which Cs^+ ions have substituted a small amount of MA^+ (8% occupancy in each MA^+), which improves the crystal symmetry leading to different space groups compared to the pristine compound. Nevertheless, the two crystals are still almost the same with similar atom positions, distances, compositions, *etc.*, which is evidenced by the similarity of the area in the red dash line and unit cell of $(MA)_4InCl_7{:}Cs^+$ in Fig. S2 (ESI†). Mn^{2+} and Sb^{3+} ions were not observed in the crystal structures of $(MA)_4InCl_7{:}Mn^{2+}$ and $(MA)_4InCl_7{:}Sb^{3+}$, probably due to the small doping ratio of Mn^{2+} and similar sizes between Sb^{3+} and In^{3+}. The experimentally measured powder X-ray diffraction (PXRD) patterns of the pristine and doped compounds display high similarity to their simulated patterns as shown in Fig. S3 (ESI†), not only suggesting the reliability of the crystal structures, but also further evidencing the unchanged crystal structures upon metal ion doping.

To determine the actual atom ratios of the doped compounds, inductively coupled plasma optical emission

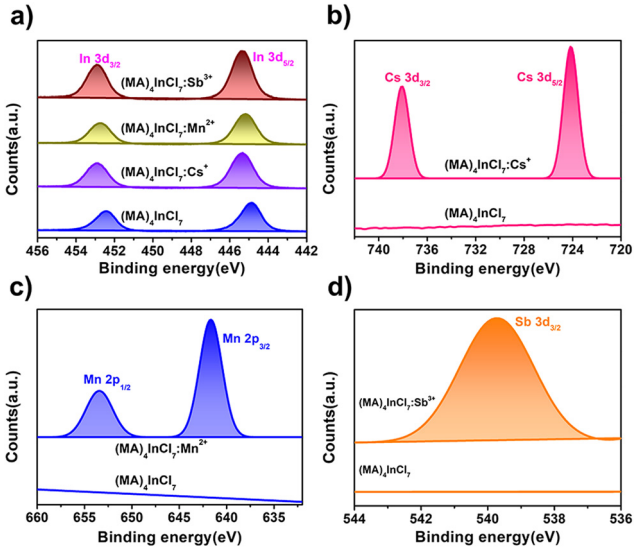

Fig. 2 High-resolution X-ray photoelectron spectroscopy (XPS) spectra of all compounds. (a) XPS spectra of In 3d in all compounds. (b) XPS spectra of Cs 3d in $(MA)_4InCl_7$ and $(MA)_4InCl_7$:Cs^+. (c) XPS spectra of Mn 2p in $(MA)_4InCl_7$ and $(MA)_4InCl_7$:Mn^{2+}. (d) XPS spectra of Sb 3d in $(MA)_4InCl_7$ and $(MA)_4InCl_7$:Sb^{3+}.

spectrometry (ICP-OES) was utilized and the experimental ratios are summarized in Table S5 (ESI†). The amount of Sb^{3+} is close to the actual experimental amount (~10%), while the experimental ratios of Cs^+ or Mn^{2+} (~2.5% and ~0.2% respectively) are much less than the feeding ratios (~5.8% and ~3.0% respectively), indicating that Sb^{3+} can be more efficiently incorporated into the crystal with a homogeneous distribution than the other dopants (Cs^+ and Mn^{2+}). Effective doping was also confirmed by X-ray photoelectron spectroscopy (XPS). As shown in Fig. 2a and Fig. S4 (ESI†), In $3d_{3/2}$ and In $3d_{5/2}$ peaks (at 452.43 and 444.88 eV) in pristine $(MA)_4InCl_7$ are shifted to higher binding energy by 0.50, 0.40 and 0.45 eV upon Cs^+, Mn^{2+} and Sb^{3+} doping, respectively. Accordingly, the peaks of Cs $3d_{3/2}$ and Cs $3d_{5/2}$ (738.1 and 724.2 eV), Mn 2p1/2 and Mn $2p_{3/2}$ (653.5 and 641.6 eV) and Sb $3d_{3/2}$ (539.9 eV) are observed in $(MA)_4InCl_7$:Cs^+, $(MA)_4InCl_7$:Mn^{2+} and $(MA)_4InCl_7$:Sb^{3+} respectively, verifying the presence of doped ions in the crystals (Fig. 2b–d).

The PL properties of all compounds were characterized by steady state and time-resolved emission spectroscopy, which are summarized in Table 1. We compare the photophysical properties of $(MA)_4InCl_7$ with $(MA)_4InCl_7$:Cs^+ and $(MA)_4InCl_7$:Mn^{2+} first. $(MA)_4InCl_7$ exhibits a broadband blue

Table 1 Photophysical properties of all compounds at room temperature

Materials	Optical band gap(eV)	λ_{exc} (nm)	λ_{em} (nm)	FWHM (nm)	PLQE (%)	τ (ns)
$(MA)_4InCl_7$	3.34	273, 366	455	152	11.2	6.72
$(MA)_4InCl_7$:Cs^+	3.36	298, 359	445	139	18.8	6.53
$(MA)_4InCl_7$:Mn^{2+}	3.00	278, 363	445	114	20.7	7.94
$(MA)_4InCl_7$:Sb^{3+}	3.23	283, 323	611	164	74.7	5420

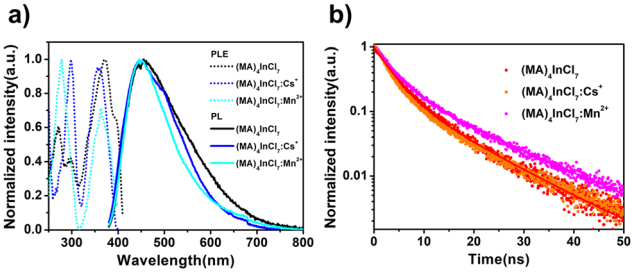

Fig. 3 (a) Excitation and emission spectra of $(MA)_4InCl_7$, $(MA)_4InCl_7$:Cs^+ and $(MA)_4InCl_7$:Mn^{2+}. (b) Time-resolved PL decays of $(MA)_4InCl_7$, $(MA)_4InCl_7$:Cs^+ and $(MA)_4InCl_7$:Mn^{2+}.

emission peaked at 455 nm with a PLQE of 11.2% when excited by 365 nm UV light as shown in Fig. 3a. The large Stokes shift and broadband emission suggest a self-trapped exciton mechanism, in which the generated excitons go through exciton–phonon interactions into self-trapped states (STE) with lower energy as commonly observed in other 0D OIMHs.[38–41] Cs^+ and Mn^{2+} doping slightly blue-shifts and narrows the blue emission peak. This phenomenon could have possibly originated from either the less extent of exciton–phonon coupling strength or more homogenous crystal structure. Given that the experimental crystal structures remain almost unchanged upon doping, the latter reason is more likely. Interestingly, the PLQE is significantly enhanced to 18.8% and 20.7% for Cs^+ doping and Mn^{2+} doping, respectively, which is not reported for other 0D indium OIMHs before.

Furthermore, the PL decay dynamics of $(MA)_4InCl_7$, $(MA)_4InCl_7$:Cs^+ and $(MA)_4InCl_7$:Mn^{2+} are characterized by time-resolved PL (TRPL) spectroscopy at room temperature (Fig. 3b). The PL decay curves can be well fitted using a bi-exponential fitting function as follows:

$$I(t) = A_1 \exp\left(-\frac{t}{\tau_1}\right) + A_2 \exp\left(-\frac{t}{\tau_2}\right) + y_0$$

where τ_1 and τ_2 represent the lifetimes of two different decay components, and A_1 and A_2 are their weighted amplitudes.

As shown in Table S6 (ESI†), the short lifetime τ_1 and the long lifetime τ_2 for all three compounds lie in the range of 2–3 ns (81–84%) and 11–12 ns (19–16%) respectively, resulting in an average PL decay lifetime of 6–7 ns. We attribute the fast decay and the slow decay components to the non-radiative and radiative recombination processes of the excitons, respectively. The faster decay through the non-radiative channel with a larger weighted amplitude could well explain the relatively low PLQE of the three compounds. Also, the radiative recombination rate an a nanosecond scale implies that the emission may be classified as fluorescence originating from singlet excitons. Together with the possible STE emission mechanism, the blue emission of $(MA)_4InCl_7$, $(MA)_4InCl_7$:Cs^+ and $(MA)_4InCl_7$:Mn^{2+} could be attributed to the ^{1}STE to $^1S_0$ transition of In^{3+} (Fig. 4e), which could be confirmed from the density functional theory (DFT) calculations in the following section.

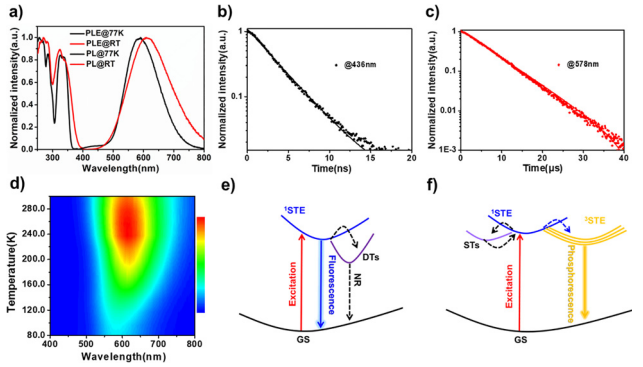

Fig. 4 (a) The excitation (probed at the corresponding emission wavelengths) and emission (excited by 280 nm UV light) spectra of $(MA)_4InCl_7:Sb^{3+}$ at room temperature and 77 K. (b and c) Time-resolved decay curves monitored at 436 nm and 578 nm, respectively. (d) Temperature-dependent emission spectra upon excitation at 280 nm. (e) Schematic illustration of the light-emitting mechanism of $(MA)_4InCl_7$, $(MA)_4InCl_7:Cs^+$ and $(MA)_4InCl_7:Mn^{2+}$. (f) Schematic illustration of the light-emitting mechanism of $(MA)_4InCl_7:Sb^{3+}$.

When it comes to the Sb^{3+} doped compound $(MA)_4InCl_7:Sb^{3+}$, the emission mechanism is a totally different story. Upon Sb^{3+} doping, partial substitution of $InCl_6^{3-}$ to $SbCl_6^{3-}$ was anticipated, due to the similar size and chemical reactivity of the two elements. Compared with that of the pristine $(MA)_4InCl_7$, the emission peak of $(MA)_4InCl_7:Sb^{3+}$ significantly red-shifted to 611 nm, with the PLQE greatly enhanced to 74.7%. This orange emission is likely to originate from the STE emission from the $SbCl_6^{3-}$ moiety suggested by previously reported 0D antimony OIMHs and antimony doped 0D indium OIMHs.[15,42,43] To prove that, the excitation wavelength–dependent PL spectra of $(MA)_4InCl_7:Sb^{3+}$ were first collected at room temperature. There is not much variation in the PL spectra excited at different wavelengths (from 250 to 360 nm) at room temperature, which confirms that the orange emission stems from the same excited states (Fig. S5, ESI†). The large Stokes shift of 170 nm and the broadband emission are typical characteristics of STE emissions.

Temperature-dependent PL spectra were further obtained to confirm the photoluminescence mechanism by monitoring the electron dynamics of the excited states. As shown in Fig. 4a, there emerges another emission peak located at 436 nm when the temperature was lowered to 77 K (excited by 280 nm UV light), which is not observed at room temperature. According to previous studies, the first excited state of OIMHs with $5s^2Sb^{3+}$ could split into a singlet state ($^1P_1$) and triplet states (^3P_n, $n = 0$, 1, and 2) and then go through lattice distortion to form self-trapped excitons.[44,45] The ^{1}STE to ^{3}STE transition of Sb^{3+} was suspended when the temperature was lowered to 77 K due to the energy barrier between the two states, resulting in dual emission at 77 K. The lifetimes of 4.65 ns for the 436 nm emission peak and 6.11 μs for the 578 nm emission peak clearly evidence the fast and slow transitions of $^1STE \rightarrow {}^1S_0$ and $^3STE \rightarrow {}^1S_0$ respectively (Fig. 4b and c). Therefore, the orange emission of $(MA)_4InCl_7:Sb^{3+}$ has originated from the ^{3}STE of $SbCl_6^{3+}$ as a result of metal ion substitution and fast ^{1}STE to ^{3}STE transition at room temperature (Fig. 4f). In addition, the absence of emission from $InCl_6^{3-}$ in $(MA)_4InCl_7:Sb^{3+}$ implies efficient energy transfer from excited $InCl_6^{3-}$ to $SbCl_6^{3-}$.

A negative thermal quenching effect was observed for the 578 nm peak of $(MA)_4InCl_7:Sb^{3+}$ in the temperature-dependent PL spectra. As shown in Fig. 4d, the peak intensity first increases and then decreases when the temperature increases from 77 K to 297 K. This can be explained by the existence of shallow traps (STs) in 0D OIMHs as suggested by Sun *et al.*[46] The excitons in the shallow traps could be thermally activated to detrap into the STE of $(MA)_4InCl_7:Sb^{3+}$ to increase the emission intensity (Fig. 4f). It's intriguing that the negative thermal quenching effect was not observed for $(MA)_4InCl_7$, $(MA)_4InCl_7:Cs^+$ and $(MA)_4InCl_7:Mn^{2+}$. This may imply that they possess deeper traps that excitons could not detrap at room temperature. The shallow/deep traps in these 0D indium OIMHs could explain the dramatic enhancement of PLQE when $(MA)_4InCl_7$ was doped with Sb^{3+}.

We found a big difference in the crystal morphologies between the pristine and doped ones using a UV-microscope. The photographs of the four compounds under ambient and UV light are shown in Fig. 5a–h. We observed that the doped crystals are more regular-shaped and transparent with fewer bulk defects compared with the parental $(MA)_4InCl_7$. This indicates that metal ion doping can improve the crystal quality and reduce bulk defects. The defect passivation effect introduced by metal ion doping may be an imperative reason for the PLQE enhancement in these 0D OIMHs due to the reduced trap-assisted non-radiative recombination centers. Better crystal quality also results in a more homogenous crystal structure, which is supported by the UV absorption spectra of the four compounds. As shown in Fig. S6 (ESI†), $(MA)_4InCl_7$, $(MA)_4InCl_7:Cs^+$ and $(MA)_4InCl_7:Mn^{2+}$ exhibit various degrees of Urbach tails which indicate that there are a certain number of sub-band-gap states underneath the conduction band of each structure upon photoexcitation, which could be the result of defects, structural disorders or inhomogeneity of crystals.[47–51] When passivated by Cs^+ and Mn^{2+}, the sub-band-gap states of $(MA)_4InCl_7$ should partially diminished, explaining the reduced FWHM and increased PLQE. A very small Urbach tail was observed for $(MA)_4InCl_7:Sb^{3+}$, suggesting minimized sub-band-gap states and homogenous crystals with less

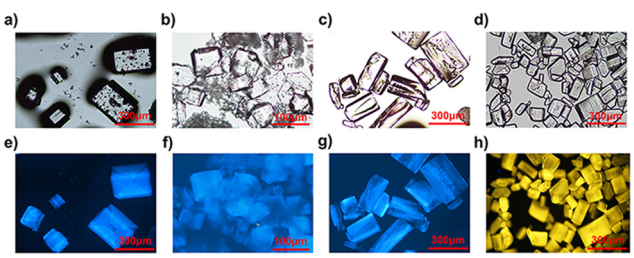

Fig. 5 (a–d) Crystal morphologies of $(MA)_4InCl_7$, $(MA)_4InCl_7:Cs^+$, $(MA)_4InCl_7:Mn^{2+}$ and $(MA)_4InCl_7:Sb^{3+}$ under visible light, respectively. (e–h) Their crystal morphologies under 365 nm UV light, respectively.

defects. Less defect-mediated degradation may explain the high stability of $(MA)_4InCl_7$:Sb^{3+}, which maintained a high PLQE when stored under ambient or under continuous UV irradiation for 4 days (Fig. S7, ESI†).

To validate the origin of the emission from the four compounds, we calculated the electronic band structure and partial density of states (PDOS) of $(MA)_4InCl_7$, $(MA)_4InCl_7$:Cs^+, $(MA)_4InCl_7$:Mn^{2+} and $(MA)_4InCl_7$:Sb^{3+} using density functional theory as shown in Fig. 6. Models of $(MA)_4InCl_7$:Cs^+ and $(MA)_4InCl_7$:Mn^{2+} for DFT calculations were built by partially replacing MA^+ by Cs^+ and Mn^{2+} (two MA^+ were replaced by one Mn^{2+} for charge balance) respectively, which could be regarded as the doped Cs^+ and Mn^{2+} occupying the defect sites of MA^+ vacancy. The model of $(MA)_4InCl_7$:Sb^{3+} for DFT calculations was based on partial substitution of In^{3+} by Sb^{3+}. The single crystal structures of these models are listed in Fig. S8 (ESI†) and the calculated band structures of these four compounds are shown in Fig. S9 (ESI†). The calculated band gaps of $(MA)_4InCl_7$ and $(MA)_4InCl_7$:Cs^+ are consistent with their experimental values, while the calculated band gaps of $(MA)_4InCl_7$:Mn^{2+} and $(MA)_4InCl_7$:Sb^{3+} are expected to be underestimated due to the well-known PBE band gap error. Nevertheless, the decreased band gaps upon Mn^{2+} and Sb^{3+} doping follow the trend of the calculation results. $(MA)_4InCl_7$ exhibits a slightly indirect bandgap of 3.36 eV. The flat conduction band and valence band indicate large effective mass of charges and localized electronic states commonly observed in other 0D OIMHs. The calculated partial density of states suggest that the valence band maximum (VBM) is comprised mostly of Cl 3p, while the conduction band minimum (CBM) is the hybrid of In 5s and Cl 3p orbitals. The contribution of MA^+ organic moieties to the band structure is negligible. Therefore, the excitation of $(MA)_4InCl_7$ should lead to a self-trapped exciton localized on the $InCl_6^{3-}$ inorganic moiety, which in turn distorts its structural conformation. The band structure of $(MA)_4InCl_7$:Cs^+ is almost identical to that of $(MA)_4InCl_7$, suggesting that Cs^+ was not involved in the electron transition of the blue emission. In contrast, Mn^{2+} doping introduced mid-gap states, lowering the theoretical bandgap to 2.07 eV. It was reported that doped Mn^{2+}could exhibit red emission arising from the d–d electron transition,[12,52–55] which could be the origin of the PL intensity increase at ~650 nm in Fig. 3a and the absorption increase at 330 nm in Fig. S6 (ESI†). However, these changes of photoluminescent properties upon Mn^{2+} doping are limited due to the small doping ratio of Mn^{2+}. The blue emission of $(MA)_4InCl_7$:Mn^{2+} should have the same origin as $(MA)_4InCl_7$ and the dramatic PLQE enhancement upon Mn^{2+} doping should come from defect passivation and better crystal quality as analyzed above. Combined with the TRPL results, we conclude that $(MA)_4InCl_7$, $(MA)_4InCl_7$:Cs^+ and $(MA)_4InCl_7$:Mn^{2+} share the same light-emitting mechanism, in which the broadband blue emission with large Stokes shift is the manifestation of the radiative recombination of the singlet excitons from the self-trapped excited states of In^{3+} (Fig. 4e). On the other hand, Sb^{3+} doping also introduced mid-gap states which lowers the bandgap to 2.31 eV. Evidenced by the PL properties and negative thermal quenching effect, the high PLQE of $(MA)_4InCl_7$:Sb^{3+} could be attributed to the highly efficient radiative recombination of ^{3}STE on $SbCl_6^{3-}$ and the absence of deep trap states (Fig. 4f).

As mentioned above, the pristine $(MA)_4InCl_7$ exhibits intense blue emission but quickly turned to orange after the reaction with Sb^{3+}, which makes it a promising antimony ion sensor. To prove this concept, a demo sensor was simply made by mixing $(MA)_4InCl_7$ powder with ethanol which do not dissolve the compound. As shown in Fig. 7a, when a small amount of dilute Sb^{3+} ethanol solution was added to the sensor, the emission under UV rapidly switched to orange accompanied by the PL intensity increase. The working curve of the sensor was measured by correlating the PL intensity of the 610 nm emission with the concentration of Sb^{3+}, which shows a near-linear relationship beneficial for the quantitative analysis. This sensor also exhibits an ultra-low detection limit of 0.1 mM (22.8 ppm) for antimony metal ions, and a fast responsive time of up to 15 s in the working region. We also tested its selectivity by adding solution of other metal ions (Pb^{2+} and Bi^{3+}), which introduces little changes to its PL spectrum as shown in

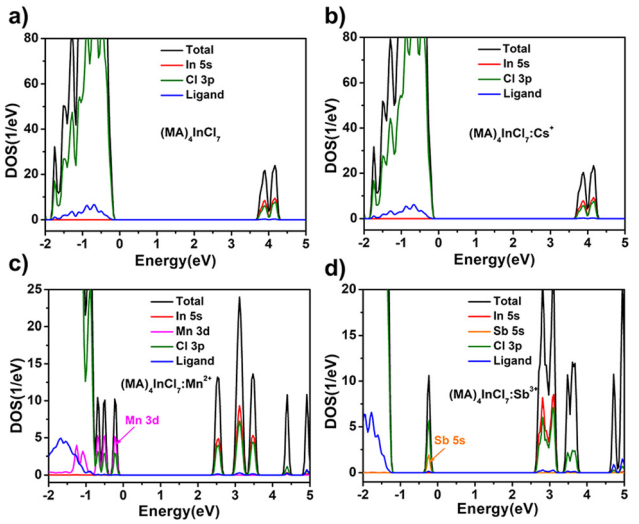

Fig. 6 Partial density of states of (a) $(MA)_4InCl_7$, (b) $(MA)_4InCl_7$:Cs^+, (c) $(MA)_4InCl_7$:Mn^{2+} and (d) $(MA)_4InCl_7$:Sb^{3+}.

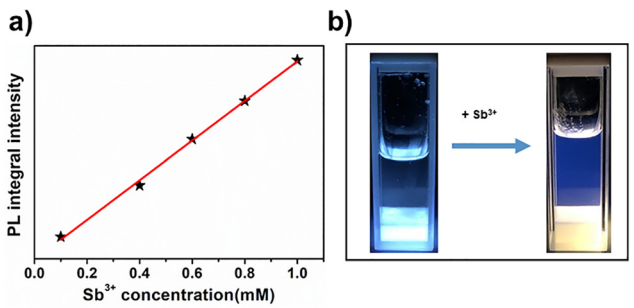

Fig. 7 (a) The sensor demo and the PL change after adding Sb^{3+} ethanol solution (excited by 365 nm UV light). (b) Working curve of the Sb^{3+} sensor.

Fig. S11 (ESI†), suggesting that the sensor is highly selective for Sb^{3+} among other heavy metal ions.

Conclusions

In summary, we have developed a series of lead-free 0D indium OIMHs including pristine $(MA)_4InCl_7$ and its doped compounds $(MA)_4InCl_7$:Cs^+, $(MA)_4InCl_7$:Mn^{2+}, and $(MA)_4InCl_7$:Sb^{3+}. The blue emission of $(MA)_4InCl_7$, $(MA)_4InCl_7$:Cs^+ and $(MA)_4InCl_7$:Mn^{2+} originates from ^{1}STE of its inorganic moiety $InCl_6^{3-}$, as determined from experimental characterization and theoretical calculations. By using a metal ion doping strategy, both narrower blue emission and a significantly increased PLQE of up to 18.8% (Cs^+ doping) or 20.7% (Mn^{2+} doping) have been achieved, which are attributed to the defect passivation effect and homogenous crystal growth. Moreover, 7-fold PLQE enhancement and shifted orange emission were realized through Sb^{3+} doping. The divergent emission originates from ^{3}STE of the altered emission center $SbCl_6^{3-}$ which makes it a promising candidate for antimony ion sensing. Our work not only proposes several efficient lead-free blue light-emitting materials, but also shows the potential of the metal ion doping strategy in achieving PLQE enhancement and emission spectrum manipulation. We also unprecedently demonstrated a new application of organic indium halide as a metal ion sensor.

Author contributions

Lin F, Yu G and Weng S designed and synthesized the samples, performed characterization and investigated the references; Zhou C and Han Y helped to analyze the data; Zhou K collected and analyzed the single crystal X-ray diffraction data. Lin F wrote the paper with support from Lin H, Liu W and Wang Y. Lin H supervised the project and revised the article. All authors contributed to the general discussion.

Conflicts of interest

There are no conflicts to declare.

Acknowledgements

We thank the National Natural Science Foundation of China (22005202) and the Scientific Research Startup Fund for Shenzhen High-Caliber Personnel of SZPT (6022310054k) for financial support.

References

1 C. Wang, Y. Zhang, F. Gu, Z. Zhao, H. Li, H. Jiang, Z. Bian and Z. Liu, Illumination Durability and High-Efficiency Sn-Based Perovskite Solar Cell under Coordinated Control of Phenylhydrazine and Halogen Ions, *Matter*, 2021, **4**, 709–721.
2 R. Gao, M. S. Kodaimati and D. Yan, Recent Advances in Persistent Luminescence Based on Molecular Hybrid Materials, *Chem. Soc. Rev.*, 2021, **50**, 5564–5589.
3 Y. Wang, L. Song, Y. Chen and W. Huang, Emerging New-Generation Photodetectors Based on Low-Dimensional Halide Perovskites, *ACS Photonics*, 2020, **7**, 10–28.
4 T. Wu, Y. Wang, X. Li, Y. Wu, X. Meng, D. Cui, X. Yang and L. Han, Efficient Defect Passivation for Perovskite Solar Cells by Controlling the Electron Density Distribution of Donor-pi-Acceptor Molecules, *Adv. Energy Mater.*, 2019, **9**, 1803766.
5 G. Weng, J. Tian, S. Chen, J. Xue, J. Yan, X. Hu, S. Chen, Z. Zhu and J. Chu, Giant Reduction of the Random Lasing Threshold in $CH_3NH_3PbBr_3$ Perovskite Thin Films by Using a Patterned Sapphire Substrate, *Nanoscale*, 2019, **11**, 10636–10645.
6 M. H. Park, J. S. Kim, J. M. Heo, S. Ahn, S. H. Jeong and T. W. Lee, Boosting Efficiency in Polycrystalline Metal Halide Perovskite Light-Emitting Diodes, *ACS Energy Lett.*, 2019, **4**, 1134–1149.
7 D. B. Velusamy, M. A. Haque, M. R. Parida, F. Zhang and T. Wu, O. F. Mohammed and H. N. Alshareef, 2D Organic-Inorganic Hybrid Thin Films for Flexible UV-Visible Photodetectors, *Adv. Funct. Mater.*, 2017, **27**, 1605554.
8 T. Xu, Y. Li, M. Nikl, R. Kucerkova, Z. Zhou, J. Chen, Y.-Y. Sun, G. Niu, J. Tang, Q. Wang, G. Ren and Y. Wu, Lead-Free Zero-Dimensional Organic-Copper(I) Halides as Stable and Sensitive X-ray Scintillators, *ACS Appl. Mater. Interfaces*, 2022, **14**, 14157–14164.
9 G. M. Song, Z. Y. Li, P. F. Gong, R. J. Xie and Z. S. Lin, Tunable White Light Emission in a Zero-Dimensional Organic-Inorganic Metal Halide Hybrid with Ultra-High Color Rendering Index, *Adv. Opt. Mater.*, 2021, **9**, 7.
10 M. D. Smith, B. A. Connor and H. I. Karunadasa, Tuning the Luminescence of Layered Halide Perovskites, *Chem. Rev.*, 2019, **119**, 3104–3139.
11 S. Sun, M. Lu, X. Gao, Z. Shi, X. Bai, W. W. Yu and Y. Zhang, 0D Perovskites: Unique Properties, Synthesis, and Their Applications, *Adv. Sci.*, 2021, **8**, 2102689.
12 G. Zhou, J. Ding, X. Jiang, J. Zhang, M. S. Molokeev, Q. Ren, J. Zhou, S. Li and X.-M. Zhang, Coordination Units of Mn^{2+} Modulation Toward Tunable Emission in Zero-Dimensional Bromides for White Light-Emitting Diodes, *J. Mater. Chem. C*, 2022, **10**, 2095–2102.
13 G. J. Zhou, Z. Y. Liu, J. L. Huang, M. S. Molokeev, Z. W. Xiao, C. G. Ma and Z. G. Xia, Unraveling the Near-Unity Narrow-Band Green Emission in Zero-Dimensional Mn^{2+}-Based Metal Halides: A Case Study of $(C_{10}H_{16}N)_2Zn_{1-x}Mn_xBr_4$ Solid Solutions, *J. Phys. Chem. Lett.*, 2020, **11**, 5956–5962.
14 Q. Wei, T. Chang, R. Zeng, S. Cao, J. Zhao, X. Han, L. Wang and B. Zou, Self-Trapped Exciton Emission in a Zero-Dimensional $(TMA)_2SbCl_5$·DMF Single Crystal and Molecular Dynamics Simulation of Structural Stability, *J. Phys. Chem. Lett.*, 2021, **12**, 7091–7099.
15 J. L. Li, Y. F. Sang, L. J. Xu, H. Y. Lu, J. Y. Wang and Z. N. Chen, Highly Efficient Light-Emitting Diodes Based on

an Organic Antimony(III) Halide Hybrid, *Angew. Chem., Int. Ed.*, 2022, **61**, e202113450.

16 L. Lian, P. Zhang, X. Zhang, Q. Ye, W. Qi, L. Zhao, J. Gao, D. Zhang and J. Zhang, Realizing Near-Unity Quantum Efficiency of Zero-Dimensional Antimony Halides through Metal Halide Structural Modulation, *ACS Appl. Mater. Interfaces*, 2021, **13**, 58908–58915.

17 C. Zhou, H. Lin, Y. Tian, Z. Yuan, R. Clark, B. Chen, L. J. van de Burgt, J. C. Wang, Y. Zhou, K. Hanson, Q. J. Meisner, J. Neu, T. Besara, T. Siegrist, E. Lambers, P. Djurovich and B. Ma, Luminescent Zero-Dimensional Organic Metal Halide Hybrids with Near-Unity Quantum Efficiency, *Chem. Sci.*, 2018, **9**, 586–593.

18 C. Sun, K. Jiang, M. F. Han, M. J. Liu, X. K. Lian, Y. X. Jiang, H. S. Shi, C. Y. Yue and X. W. Lei, A Zero-Dimensional Hybrid Lead Perovskite with Highly Efficient Blue-Violet Light Emission, *J. Mater. Chem. C*, 2020, **8**, 11890–11895.

19 H. Lin, C. Zhou, M. Chaaban, L. J. Xu, Y. Zhou, J. Neu, M. Worku, E. Berkwits, Q. He, S. Lee, X. Lin, T. Siegrist, M. H. Du and B. Ma, Bulk Assembly of Zero-Dimensional Organic Lead Bromide Hybrid with Efficient Blue Emission, *ACS Mater. Lett.*, 2019, **1**, 594–598.

20 C. Zhou, H. Lin, M. Worku, J. Neu, Y. Zhou, Y. Tian, S. Lee, P. Djurovich, T. Siegrist and B. Ma, Blue Emitting Single Crystalline Assembly of Metal Halide Clusters, *J. Am. Chem. Soc.*, 2018, **140**, 13181–13184.

21 R. Roccanova, A. Yangui, H. Nhalil, H. Shi, M.-H. Du and B. Saparov, Near-Unity Photoluminescence Quantum Yield in Blue-Emitting $Cs_3Cu_2Br_{5-x}I_x$ ($0 \leq x \leq 5$), *ACS Appl. Electron. Mater.*, 2019, **1**, 269–274.

22 T. Jun, K. Sim, S. Iimura, M. Sasase, H. Kamioka, J. Kim and H. Hosono, Lead-Free Highly Efficient Blue-Emitting $Cs_3Cu_2I_5$ with 0D Electronic Structure, *Adv. Mater.*, 2018, **30**, e1804547.

23 J. Li, T. Inoshita, T. Ying, A. Ooishi, J. Kim and H. Hosono, A Highly Efficient and Stable Blue-Emitting $Cs_5Cu_3Cl_6I_2$ with a 1D Chain Structure, *Adv. Mater.*, 2020, **32**, e2002945.

24 Z. Zhou, Y. Li, Z. Xing, Z. Li, K. S. Wong and J. E. Halpert, Potassium and Rubidium Copper Halide A_2CuX_3 (A = K, Rb, X = Cl, Br) Micro- and Nanocrystals with Near Unity Quantum Yields for White Light Applications, *ACS Appl. Nano Mater.*, 2021, **4**, 14188–14196.

25 T. D. Creason, T. M. McWhorter, Z. Bell, M.-H. Du and B. Saparov, K_2CuX_3 (X = Cl, Br): All-Inorganic Lead-Free Blue Emitters with Near-Unity Photoluminescence Quantum Yield, *Chem. Mater.*, 2020, **32**, 6197–6205.

26 P. Li, X. Liu, Y. Zhang, C. Liang, G. Chen, F. Li, M. Su, G. Xing, X. Tao and Y. Song, Low-Dimensional Dion-Jacobson-Phase Lead-Free Perovskites for High-Performance Photovoltaics with Improved Stability, *Angew. Chem., Int. Ed.*, 2020, **59**, 6909–6914.

27 C. Ni, G. Hedley, J. Payne, V. Svrcek, C. McDonald, L. K. Jagadamma, P. Edwards, R. Martin, G. Jain, D. Carolan, D. Mariotti, P. Maguire, I. Samuel and J. Irvine, Charge Carrier Localised in Zero-Dimensional $(CH_3NH_3)_3Bi_2I_9$ Clusters, *Nat. Commun.*, 2017, **8**, 170.

28 S. Feng, Y. Ma, S. Wang, S. Gao, Q. Huang, H. Zhen, D. Yan, Q. Ling and Z. Lin, Light/Force-Sensitive 0D Lead-Free Perovskites: From Highly Efficient Blue Afterglow to White Phosphorescence with Near-Unity Quantum Efficiency, *Angew. Chem., Int. Ed.*, 2022, e202116511, DOI: **10.1002/anie.202116511**.

29 J. H. Wei, J. F. Liao, L. Zhou, J. B. Luo, X. D. Wang and D. B. Kuang, Indium-Antimony-Halide Single Crystals for High-Efficiency White-Light Emission and Anti-counterfeiting, *Sci. Adv.*, 2021, **7**, 9.

30 Y. Zhang, S. Yuan, Y. Yuan, Y. Bao, Q. Ran, E. Liu, J. Fan and W. Li, Alleviation of π–π* Transition Enabling Enhanced Luminescence in Emerging TpyInClx (x = 3, 5) Perovskite Single Crystals, *Adv. Opt. Mater.*, 2021, **10**, 2102041.

31 Y. Y. Ma, H. Q. Fu, X. L. Liu, Y. M. Sun, Q. Q. Zhong, W. J. Xu, X. W. Lei, G. D. Liu and C. Y. Yue, Zero-Dimensional Organic–Inorganic Hybrid Indium Chlorides with Intrinsic Blue Light Emissions, *Inorg. Chem.*, 2022, **61**, 8977–8981.

32 D. Chen, S. Hao, G. Zhou, C. Deng, Q. Liu, S. Ma, C. Wolverton, J. Zhao and Z. Xia, Lead-Free Broadband Orange-Emitting Zero-Dimensional Hybrid $(PMA)_3InBr_6$ with Direct Band Gap, *Inorg. Chem.*, 2019, **58**, 15602–15609.

33 Z. Li, G. Song, Y. Li, L. Wang, T. Zhou, Z. Lin and R. J. Xie, Realizing Tunable White Light Emission in Lead-Free Indium(III) Bromine Hybrid Single Crystals through Antimony(III) Cation Doping, *J. Phys. Chem. Lett.*, 2020, **11**, 10164–10172.

34 Y. Wu, C. M. Shi, L. J. Xu, M. Yang and Z. N. Chen, Reversible Luminescent Vapochromism of a Zero-Dimensional Sb^{3+}-Doped Organic-Inorganic Hybrid, *J. Phys. Chem. Lett.*, 2021, **12**, 3288–3294.

35 D. Cortecchia, S. Neutzner, A. R. Srimath Kandada, E. Mosconi, D. Meggiolaro, F. De Angelis, C. Soci and A. Petrozza, Broadband Emission in Two-Dimensional Hybrid Perovskites: The Role of Structural Deformation, *J. Am. Chem. Soc.*, 2017, **139**, 39–42.

36 R. Zhang, X. Mao, Y. Yang, S. Yang, W. Zhao, T. Wumaier, D. Wei, W. Deng and K. Han, Air-Stable, Lead-Free Zero-Dimensional Mixed Bismuth-Antimony Perovskite Single Crystals with Ultra-broadband Emission, *Angew. Chem., Int. Ed.*, 2019, **58**, 2725–2729.

37 B. M. Benin, D. N. Dirin, V. Morad, M. Woerle, S. Yakunin, G. Raino, O. Nazarenko, M. Fischer, I. Infante and M. V. Kovalenko, Highly Emissive Self-Trapped Excitons in Fully Inorganic Zero-Dimensional Tin Halides, *Angew. Chem., Int. Ed.*, 2018, **57**, 11329–11333.

38 M. Li and Z. Xia, Recent progress of zero-dimensional luminescent metal halides, *Chem. Soc. Rev.*, 2021, **50**, 2626–2662.

39 D. Chen, S. Hao, L. Fan, Y. Guo, J. Yao, C. Wolverton, M. G. Kanatzidis, J. Zhao and Q. Liu, Broad Photoluminescence and Second-Harmonic Generation in the Noncentrosymmetric Organic-Inorganic Hybrid Halide $(C_6H_5(CH_2)_4NH_3)_4MX_7$ center dot H_2O (M = Bi, In, X = Br or I), *Chem. Mater.*, 2021, **33**, 8106–8111.

40 V. Morad, S. Yakunin and M. V. Kovalenko, Supramolecular Approach for Fine-Tuning o the Bright Luminescence from Zero-Dimensional Antimony(III) Halides, *ACS Mater. Lett.*, 2020, **2**, 845–852.

41 C. Zhou, Y. Tian, Z. Yuan, H. Lin, B. Chen, R. Clark, T. Dilbeck, Y. Zhou, J. Hurley, J. Neu, T. Besara, T. Siegrist,

P. Djurovich and B. Ma, Highly Efficient Broadband Yellow Phosphor Based on Zero-Dimensional Tin Mixed-Halide Perovskite, *ACS Appl. Mater. Interfaces*, 2017, **9**, 44579–44583.

42 J. Lin, K. Liu, H. Ruan, N. Sun, X. Chen, J. Zhao, Z. Guo, Q. Liu and W. Yuan, Zero-Dimensional Lead-Free Halide with Indirect Optical Gap and Enhanced Photoluminescence by Sb Doping, *J. Phys. Chem. Lett.*, 2022, **13**, 198–207.

43 V. Morad, S. Yakunin and M. V. Kovalenko, Supramolecular Approach for Fine-Tuning of the Bright Luminescence from Zero-Dimensional Antimony(III) Halides, *ACS Mater. Lett.*, 2020, **2**, 845–852.

44 J. Xu, S. Li, C. Qin, Z. Feng and Y. Du, Identification of Singlet Self-Trapped Excitons in a New Family of White-Light-Emitting Zero-Dimensional Compounds, *J. Mater. Chem. C*, 2020, **124**, 11625–11630.

45 K. M. McCall, V. Morad, B. M. Benin and M. V. Kovalenko, Efficient Lone-Pair-Driven Luminescence: Structure-Property Relationships in Emissive $5s^2$ Metal Halides, *ACS Mater. Lett.*, 2020, **2**, 1218–1232.

46 B. B. Zhang, J. K. Chen, J. P. Ma, X. F. Jia, Q. Zhao, S. Q. Guo, Y. M. Chen, Q. Liu, Y. Kuroiwa, C. Moriyoshi, J. Zhang and H. T. Sun, Antithermal Quenching of Luminescence in Zero-Dimensional Hybrid Metal Halide Solids, *J. Phys. Chem. Lett.*, 2020, **11**, 2902–2909.

47 X. Meng, S. Ji, Q. Wang, X. Wang, T. Bai, R. Zhang, B. Yang, Y. Li, Z. Shao, J. Jiang, K. L. Han and F. Liu, Organic-Inorganic Hybrid Cuprous-Based Metal Halides for Warm White Light-Emitting Diodes, *Adv. Sci.*, 2022, e2203596, DOI: **10.1002/advs.202203596**.

48 V. Diez-Cabanes, J. Even, D. Beljonne and C. Quarti, Electronic Structure and Optical Properties of Mixed Iodine/Bromine Lead Perovskites, *Adv. Opt. Mater.*, 2021, **9**, 2001832.

49 F. Liu, Y. Zhang, C. Ding, S. Kobayashi, T. Izuishi, N. Nakazawa, T. Toyoda, T. Ohta, S. Hayase, T. Minemoto, K. Yoshino, S. Dai and Q. Shen, Highly Luminescent Phase-Stable $CsPbI_3$ Perovskite Quantum Dots Achieving Near 100% Absolute Photoluminescence Quantum Yield, *ACS Nano*, 2017, **11**, 10373–10383.

50 S. De Wolf, J. Holovsky, S. J. Moon, P. Loper, B. Niesen, M. Ledinsky, F. J. Haug, J. H. Yum and C. Ballif, Organometallic Halide Perovskites: Sharp Optical Absorption Edge and Its Relation to Photovoltaic Performance, *J. Phys. Chem. Lett.*, 2014, **5**, 1035–1039.

51 F. Urbach, The Long-Wavelength Edge of Photographic Sensitivity and Electronic Absorption of Solids, *Phys. Rev.*, 1953, **92**, 1324–1326.

52 Z. Yu, H. Peng, Q. Wei, T. Huang, S. Yao, Y. Tian, C. Peng and B. Zou, The Magnetic Polaron Modulated Luminescence Bands of Organic-Inorganic Hybrid Ferroelectric Anti-Perovskite $(C_3H_9N)_3Cd_2Cl_7$ Doped with Mn^{2+}, *Mater. Today Chem.*, 2022, **24**, 100781.

53 S. Yan, W. Tian, H. Chen, K. Tang, T. Lin, G. Zhong, L. Qiu, X. Pan and W. Wang, Synthesis of 0D Manganese-Based Organic–Inorganic Hybrid Perovskite and Its Application in Lead-Free Red Light-Emitting Diode, *Adv. Funct. Mater.*, 2021, **31**, 2100855.

54 B. Su, G. Zhou, J. Huang, E. Song, A. Nag and Z. Xia, Mn^{2+}-Doped Metal Halide Perovskites: Structure, Photoluminescence, and Application, *Laser Photonics Rev.*, 2021, **15**, 2000334.

55 H. Yuan, F. Massuyeau, N. Gautier, A. B. Kama, E. Faulques, F. Chen, Q. Shen, L. Zhang, M. Paris and R. Gautier, Doped Lead Halide White Phosphors for Very High Efficiency and Ultra-High Color Rendering, *Angew. Chem., Int. Ed.*, 2020, **59**, 2802–2807.

